Ballistic transport in SiGe and strained Si MOSFETs

G. Curatola
Dipartimento di Ingegneria dell'Informazione: Elettronica, Informatica, Telecomunicazioni, Università di Pisa
Giuseppe Iannaccone
Dipartimento di Ingegneria dell'Informazione: Elettronica, Informatica, Telecomunicazioni, Università di Pisa

G. Curatola, G. Iannaccone, "*Ballistic transport in SiGe and strained Si MOSFETs*", Journal Computational Electronics, **2**, pp.309 -312 (2003).

Journal of Computational Electronics 2: 309–312, 2003

Ballistic Transport in SiGe and Strained-Si MOSFETs

G. CURATOLA AND G. IANNACCONE
Dipartimento di Ingegneria dell'Informazione, Università degli studi di Pisa, via Caruso, I-56122 Pisa, Italy
g.curatola@iet.unipi.it
g.iannaccone@iet.unipi.it

Abstract. We investigate the performance of bulk silicon and strained-silicon nanoscale MOSFETs in the ballistic regime, with the purpose of identifying possible advantages of silicon-germanium technology in devices approaching the ballistic regime. Investigation is performed with a 2D program that solves in a self-consistent way the Poisson equation, the Schrödinger equation with density functional theory, and the continuity equation for ballistic electrons. In the ballistic regime, when mobility has no physical meaning, strained-silicon FETs seem only to provide smaller short channel effects, but no improvement as far as transconductance and drive current are concerned.

Keywords: ballistic transport, strained-Si, MOSFET, quantum simulation

1. Introduction

Strained-silicon MOSFETs represent a very promising solution in order to prevent performance degradation in ultra-scaled devices [1]. The presence of germanium deeply affects the band structure of the semiconductor. In particular, it causes a splitting of the six-fold degenerate silicon conduction band into two-fold and four-fold degenerate valleys and hence leads to a preferential occupation of conduction band minima and to reduced intervalley scattering. In addition, changes induced in the conduction band curvature significantly reduce electron effective masses [2]. A separation between the heavy and light hole bands and an increased curvature of both bands give rise to similar effects for holes [3]. A qualitative picture of the effect of strain in Si is given in Fig. 1, where the conduction band and the first longitudinal and transverse subband in the middle of the channel are shown for a bulk silicon and for a strained-Si MOSFET with oxide thickness 1.5 nm and strained-silicon channel of 10 nm grown onto a relaxed $Si_{0.8}Ge_{0.2}$ buffer layer. In the second case, the separation between the two eigenvalues is increased, with respect to the silicon counterpart, as a consequence of subband splitting. The separation between the first longitudinal subband and transverse subband increases from 90 meV to 200 meV. Thus, almost all current is due to electrons in the first two subbands of the two longitudinal conduction band minima which offer, along the current flow direction, the lower effective masses. Both the reduced effective mass and the intervalley scattering suppression, due to the augmented subband separation, are responsible for the increased carrier mobility.

As the channel length is further reduced, it is very likely for electrons to traverse the device without undergoing inelastic scattering events, even at room temperature. Hence, in the ballistic regime, where the concept of mobility becomes meaningless, the advantages of strained layers must be carefully considered. In order to investigate this aspect, we have used a two-dimensional simulator based on the self-consistent solution of the Poisson/Schrödinger and continuity equations for both electrons and holes in the case of ballistic regime [4]. In our model, the potential barrier encountered by electrons traveling from source towards the drain is modulated by the voltage applied to the gate contact and carriers obey the distribution function of the originating contact (source or drain). Only carriers with energy larger than the peak of the barrier can be transmitted from source to drain by thermionic emission, while carriers with lower energy can be considered to be in

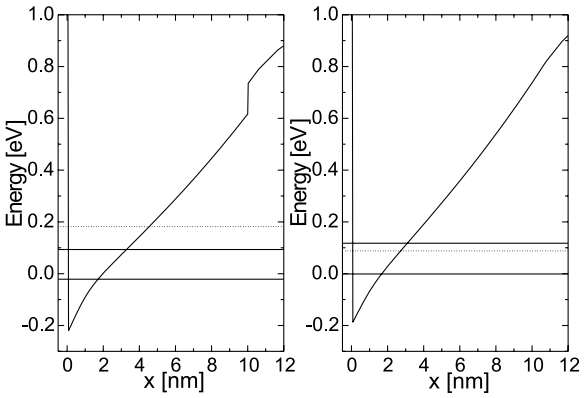

Figure 1. Conduction band profile and first two longitudinal (solid line) and first transversal subband (dashed line) in the case of bulk-silicon (right) and strained-silicon MOSFET (left). In the second case, as a consequence of the strain-induced splitting of the valleys, the separation between the first longitudinal and transversal subbands is increased.

thermal equilibrium with the closest contact (drain or source). In the present simulation, we neglect source-to-drain tunneling in the channel and assume that the transmission coefficient is unity for energies larger than the peak and zero for lower energies. A dedicated procedure allows to take into account the effects of strain on the band parameters of the material [5].

In this paper we have compared a conventional super-halo Si MOSFET with strained-Si MOSFETs, in order to assess the advantages of SiGe technology in the ballistic regime. The paper is organized as follows: In Section 2, the simulation tool used is presented and a brief discussion about the method used for calculating the electron current in the case of ballistic transport is provided. In Section 3, different Si and strained-Si nanoscale MOSFETs are discussed and the results of our simulation are presented. Finally, in Section 4 our conclusions and further discussions are presented.

2. Method

The MOSFETs considered in this paper are characterized by strong quantum confinement only in one direction (say, x). That is, we can write the density of states as a sum of two-dimensional subbands, with a profile computed by solving the Schrödinger equation in the x direction for each mesh point along the y axis. We also suppose that carriers moving from source to drain do not undergo scattering events.

Carriers are injected into the channel from a thermal equilibrium reservoir (source) and contribute to the current if they overcome the energy barrier modulated by the gate voltage and, to a lesser degree, by the drain voltage (DIBL). We simply assume that electrons with injected longitudinal energy lower than the subband maximum are reflected back to their originating contact, while the others are transmitted over the barrier and contribute to the current [6, 7].

Therefore, for each subband we evaluate the subband maximum E_{imax} and the corresponding longitudinal position y_{imax}. All electrons with longitudinal energy lower than E_{imax} are in equilibrium with the originating contact, while electrons with longitudinal energy higher than E_{imax} conserve the chemical potential of the injecting reservoir.

If we write the total energy E as $E = E_y + E_z$, where the term $E_y = E_i + \frac{\hbar^2 k_y^2}{2m_y}$ is the longitudinal energy, and $E_z = \hbar^2 k_z^2 / 2m_z$ the transverse energy, the local density of states reads:

$$N_{2D}(E_y, E_z)\, dE = 2 \sum_i |\Psi_i|^2 \frac{\sqrt{m_y m_z}}{4\pi\hbar^2} \frac{1}{\sqrt{E_y E_z}}\, dE_y\, dE_z \qquad (1)$$

where Ψ_i represents the i-th eigenfunction obtained by the Schrödinger equation, $\hbar$ is the reduced Planck constant and m_y and m_z represent the electron effective masses in the plane perpendicular to the growth direction.

The electron density is therefore given by:

$$\begin{aligned} n = & \int_0^\infty \int_0^{E_{\text{imax}} - E_i(y)} N_{2D}(E_y, E_z) \\ & \times f(E_{FS/D}, E_y + E_z) dE_y\, dE_z \\ & + \int_0^\infty \int_{E_{\text{imax}} - E_i(y)}^\infty N_{2D}(E_y, E_z) \\ & \times \left[\frac{f(E_{FS}, E_y + E_z) + f(E_{FD}, E_y + E_z)}{2} \right] dE_y\, dE_z \end{aligned} \qquad (2)$$

where $E_i(y)$ represents the i-th eigenvalue obtained by solving the Schrödinger equation for each mesh point along the y axis and $E_{FS/D}$ represents the source or drain Fermi level depending on the position of the considered grid point with respect to the value y_{imax}. This term is inserted in the right-hand side of the Poisson equation and solved, after discretization by means of the Box Integration method, self-consistently with the Schrödinger equation. The algebraic system of equations is solved with the Newton-Raphson algorithm. Since the Schrödinger equation requires large memory

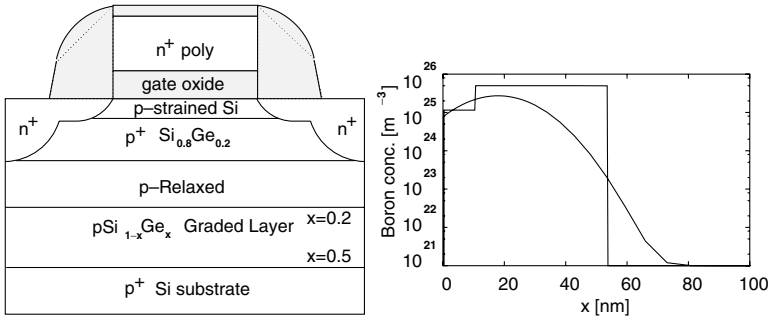

Figure 2. Strained-Si MOSFET with oxide thickness 1.5 nm and channel thickness 10 nm (left). Two different doping are considered: a super-halo p-doping in order to reduce the short channel effects and an epilayer p-doping (right).

occupancy and slows down the speed of convergence of the algorithm, we have used a simplified version of the predictor-corrector scheme [8].

After the exact solution has been obtained, the electron current is evaluated assuming that there is no tunnel current through the barrier so that only the electrons with longitudinal energy higher than E_{imax} can contribute. In particular:

$$J = \sum_i \int_{E_{\text{imax}}-E_i(y)}^{\infty} \int_0^{\infty} 2\frac{\sqrt{m_y m_z}}{h^2} \frac{1}{\sqrt{E_y E_z}} \times \sqrt{\frac{2E_y}{m_y}} \left[\frac{1}{1+\exp\left(\frac{E_y+E_z-E_{FS}}{k_B T}\right)} - \frac{1}{1+\exp\left(\frac{E_y+E_z-E_{FD}}{k_B T}\right)} \right] dE_y\, dE_z \tag{3}$$

3. Results and Discussions

We have focused our attention on three different nMOSFET structures. The first is a bulk-Si MOSFET characterized by a channel length of 25 nm and a super-halo doping in order to prevent the short channel effects [9]. The second is a strained-Si channel MOSFET with the same doping profile, fabricated on a relaxed-SiGe virtual substrate [10]. The third structure is a strained-Si MOSFET with an epitaxial SiGe p-doped layer instead of implanted super-halo p doping on the layer: we have $N_A = 1 \times 10^{19}\,\text{cm}^{-3}$ in the strained-silicon channel, $N_A = 5 \times 10^{19}\,\text{cm}^{-3}$ in the underlying SiGe layer and finally, $N_A = 10^{15}\,\text{cm}^{-3}$ in the rest of the domain. In both cases, the strained-silicon channel is 10 nm thick and a schematic representation of the structure is given in Fig. 2(left). Here it is also represented (right) the super-halo p-doping and the epitaxial p-type doping.

We have adjusted the doping dose in order to match the threshold voltage of the bulk-silicon MOS, as shown in Fig. 3, where the C-V curves for the three structures are plotted. Curves are very similar except for a small difference in the accumulation region. Furthermore, as gate voltage goes beyond 2 V, it is possible to observe the typical behavior due to poly depletion. In Fig. 4 we plot the transfer characteristics and the transconductance of the three devices for $V_{DS} = 0.5$ V and 1V. The bulk-Si MOSFET exhibits larger short channel effects leading to a lower threshold voltage. Information on the output conductance is given by the parameter λ (I_{DS} in saturation is proportional to $(1 + \lambda V_{DS})$). For the bulk-Si MOSFET we have $\lambda = 0.74\,\text{V}^{-1}$, for the super-halo SiGe MOSFET $\lambda = 0.558\,\text{V}^{-1}$ and for the epilayer SiGe MOSFET $\lambda = 0.435\,\text{V}^{-1}$, confirming improved short channel behavior for the strained-Si devices.

As far as the transconductance is concerned, however, curves seem to be only shifted, and strained-Si seems to provide no transconductance improvement.

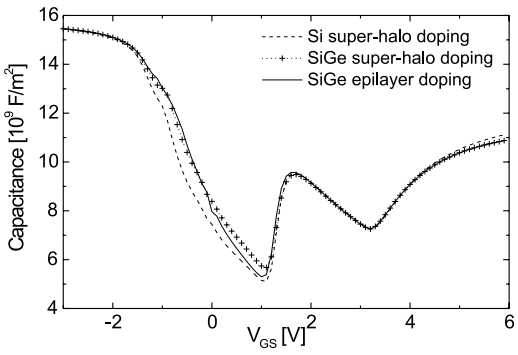

Figure 3. C-V curves for the three different MOS structures after tuning the doping profile in order to have the same threshold voltage.

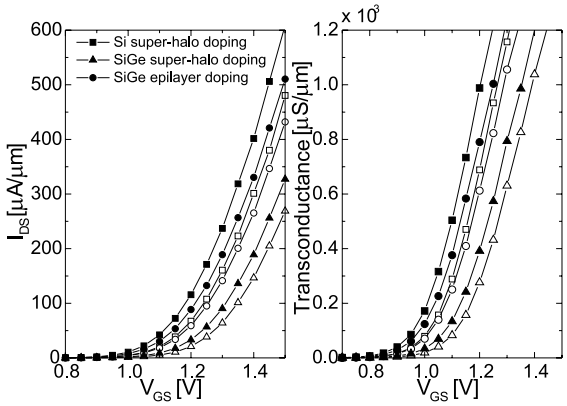

Figure 4. Transfer characteristics for Si super-halo doping, strained Si super-halo doping and strained Si epilayer doping for two different values of the source to drain voltage: 0.5 V (open symbols), 1V (solid symbols).

4. Conclusion

In the article we have presented the results of our simulations comparing the behavior of nanoscale Si and strained-Si MOSFETs in the ballistic regime. The only significant differences in the transfer characteristics are slightly more pronounced short channel effects in the silicon MOSFETs. This suggests that the current drive improvement achievable with strained-silicon devices will likely be absorbed as the ballistic regime is approached.

References

1. K. Rim, J.L. Hoyt, and J.F. Gibbons, *Elec. Dev. Meeting*, 707 (1998).
2. M. Rieger and P. Vogl, *Phys. Rev. B*, **48**, 14276 (1993).
3. D.J. Paul, *Advanced Material*, **11**, 191 (1999).
4. G. Curatola and G. Iannaccone, *J. Appl. Phys.*, to be published in Feb. 2004.
5. G. Curatola and G. Iannaccone, *Nanotechnology*, **13**, 267 (2002).
6. K. Natori, *J. Appl. Phys.*, **76**, 4879 (1994).
7. M. Lundstrom and R. Zhibin, *IEEE Trans. Elect. Dev.*, **49**, 113 (2002).
8. A. Trellakis, A.T. Galick, A. Pacelli, and U. Ravaioli, *J. Appl. Phys.*, **81**, 7880 (1997).
9. Home page of the well tempered MOSFET at MIT: www.ece.mit.edu/Well.
10. K. Rim *et al.*, *VLSI Technology*, 59 (2001).